

Gulf Stream Position, Width, and Orientation Estimated from HF Radar Radial Velocity Maps off Cape Hatteras, North Carolina

MIKE MUGLIA,^a HARVEY SEIM,^b AND PATTERSON TAYLOR^a

^a *Coastal Studies Institute, East Carolina University, Wanchese, North Carolina*

^b *Department of Marine Sciences, University of North Carolina at Chapel Hill, Chapel Hill, North Carolina*

(Manuscript received 9 July 2021, in final form 29 December 2021)

ABSTRACT: A method to extract characteristics of the Gulf Stream (GS) surface flow field using high-frequency radar (HFR)-derived currents is described. Radial velocity measurements, from radar installations near Cape Hatteras, North Carolina, serve as input, chosen because of the greater spatial and temporal coverage provided compared to total velocity fields. The landward GS edge, jet axis, orientation, and cyclonic shear zone (CSZ) width are identified along bearings within the radar footprint. The method is applied to observations from two radar installations from November 2014 and provides GS estimates with daily temporal resolution. Results along eight bearings provide a consistent representation of GS variability dominated by the passage of meanders. Average distance to the GS edge along bearings varies from 50 to 100 km; distance estimate quality degrades with range from the radars. Monthly mean GS jet axis locations from satellite sea surface height (SSH) and the algorithm are consistent. Cross correlations between estimates of GS characteristics in the same region vary from 0.37 to 0.73 for the GS edge. Estimates of radar distance to the GS edge are negatively correlated with current velocity measurements nearest the surface from a moored 150-kHz acoustic Doppler current profiler and vary between -0.58 and -0.71 . GS CSZ width metrics range from mean values of 29–31 km. Daily GS orientation estimates are affected by the crossing angle of the radial bearing relative to the GS. Lags from the cross correlations of monthly mean properties suggest meander propagation speed estimates increase from 43.2 km day^{-1} south of the cape, to $136.8 \text{ km day}^{-1}$ just east of it.

KEYWORDS: Ocean; Atlantic Ocean; Continental shelf/slope; North Atlantic Ocean: Sea/ocean surface; Boundary currents; Coastal flows; Currents; Dynamics; Ocean circulation; Ocean dynamics; Boundary currents; Acoustic measurements/effects; Algorithms; Data processing/distribution; In situ oceanic observations; Instrumentation/sensors; Measurements; Profilers; oceanic; Radars/Radar observations; Remote sensing; Surface observations; Time series

1. Introduction


High-frequency radar (HFR) installations near Cape Hatteras, North Carolina, that estimate surface currents provide consistent and more frequent Gulf Stream (GS) location and orientation estimates than previously available from other observations and provide new insights into the oceanography off Cape Hatteras. Here we present a method to determine variability in the GS's landward edge and jet axis location, orientation, and a metric for the width of the cyclonic shear zone (CSZ) (Archer et al. 2017) off North Carolina using radial velocity maps measured with monostatic 5-MHz HFR from CODAR Ocean Sensors. The method may also provide estimates of the GS separation point from the continental margin, which is believed to influence GS properties downstream of Cape Hatteras (Gangopadhyay et al. 1992; Silver et al. 2021).

a. Regional oceanography

The GS has a profound influence on the complex current dynamics off Cape Hatteras that result from the convergence of many different water masses in the region. Processes

influenced by the GS in this area include cross-isobath transport of shelf water at the convergence of Mid-Atlantic Bight (MAB) and South Atlantic Bight (SAB) shelf water (Savidge and Bane 2001), shape and position of the Hatteras Front (Savidge and Austin 2007), warm water incursions onto the MAB from warm core rings (WCR) (Zhang and Gawarkiewicz 2015), larval recruitment on the MAB related to WCRs (Myers and Drinkwater 1989), biological productivity in the SAB (Lee et al. 1991), and ocean-atmosphere interactions (Frankignoul et al. 2001). Although essential to understanding oceanography off the North Carolina coast, and to linkages beyond the region, GS variability in this area has been difficult to quantify because of the challenge involved in obtaining observations of consistent spatial and temporal resolution over long time periods.

The GS flows over the upper continental slope, following the southeastern U.S. shelf break from the Florida Straits to Cape Hatteras, where it separates abruptly from the slope, proceeding northeastward into deeper water over the abyssal plain as a free jet. Off Cape Hatteras, the GS is ~ 100 km wide and ~ 1000 m deep, with estimates highly dependent on cross-stream latitude and definition (Halkin and Rossby 1985; Hall and Bryden 1985; Hogg 1992; Watts et al. 1995; Meinen et al. 2009). The horizontal and vertical scales of the baroclinic structure have been found to be quite consistent in this area (Johns et al. 1995), notably maintaining structural consistency despite regular variations in GS position (Halkin and Rossby 1985).

 Denotes content that is immediately available upon publication as open access.

Corresponding author: Mike Muglia, mugliam@ecu.edu

DOI: 10.1175/JTECH-D-21-0098.1

© 2022 American Meteorological Society. For information regarding reuse of this content and general copyright information, consult the [AMS Copyright Policy \(www.ametsoc.org/PUBSReuseLicenses\)](#).

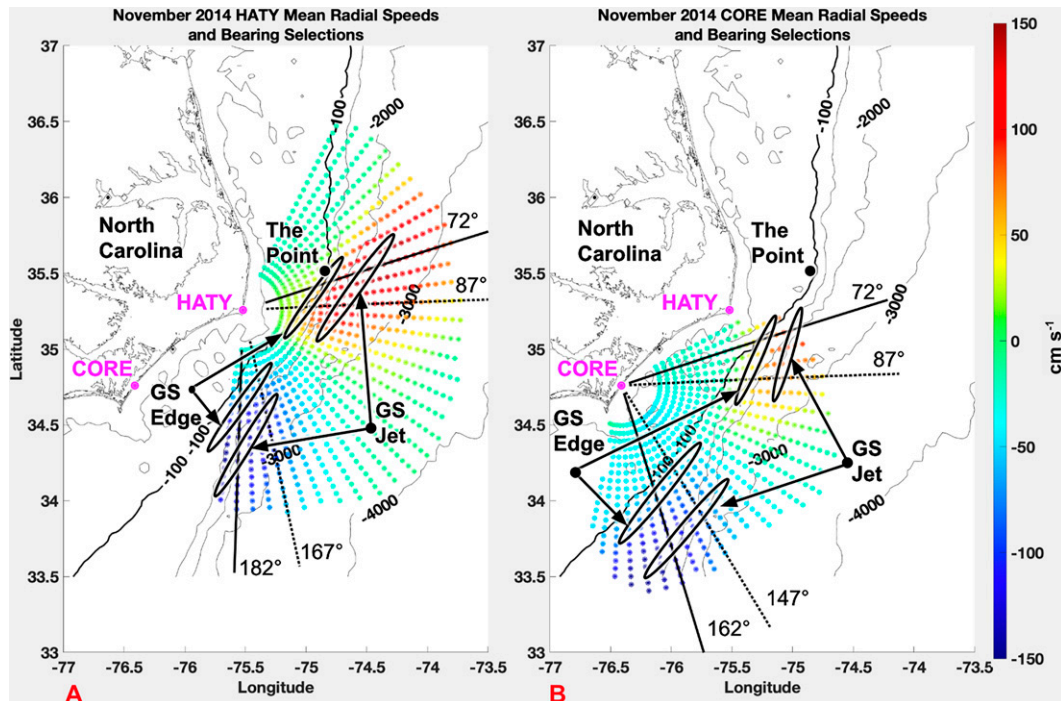


FIG. 1. (a) HATY mean radial speeds for November 2014, where observations are present more than 70% of the time, and bearings selected by the algorithm for GS analysis. “Mode bearings” are 72° and 182° and “proximal bearings” are 87° and 167° for HATY. The pink dot on land is the radar location. The locations of the GS edge and jet have been circled. (b) CORE mean radial speeds for November 2014, where observations are present more than 70% of the time, and bearings selected by the algorithm for GS analysis. The pink dot on land is the radar location. The locations of the edge and jet have been circled.

Meanders, wavelike mesoscale variability in the GS baroclinic jet with periods and wavelengths that range from 2 to 14 days and 100 to 250 km in this region (Glenn and Ebbesmeyer 1994), are an intrinsic form of variability along the length of the GS. The GS separation point from the shelf break in this area varies (Miller 1994; Joyce et al. 2000). It is a transition region for meanders, whose lateral amplitudes grow quickly to 50 km at the Charleston Bump, and decay downstream to 10 km or less as they reach Cape Hatteras (Miller 1994), then grow again further downstream to up to 100 km or more. Meander variability time scales range from 3 to 8 days near the bathymetric feature known as the Point (see Fig. 1) to several months just downstream (Savidge 2004).

GS position off North Carolina has been explored historically with sea surface temperatures (SSTs) measured from satellites (Brooks and Bane 1983), and more recently with Navy frontal charts (<https://polar.ncep.noaa.gov/global/monitor/>) that utilize satellite SSTs, information from ships of opportunity, buoy temperature readings (Miller 1994), region-specific time-limited expansive observing efforts (Churchill and Berger 1998; Muglia et al. 2020), and satellite altimetry data (Zeng and He 2016; Andres 2021). GS characteristics are often mapped using satellite sensors that can detect the large gradients in surface temperatures and surface height associated with the GS. Off Cape Hatteras, the 25-cm sea surface height (SSH) contour from satellite altimetry provides lower-frequency, ~ 10 days, estimates

of GS location (Andres 2016). Time and spatial scales of SST measurements are satellite specific, and vary in frequency from hours to several days, and in horizontal resolution from one to tens of kilometers in this region. SST measurements are degraded and obscured by cloud cover, often significantly, making consistent estimates of GS position challenging.

Measurement of the GS edge off North Carolina is further complicated by the frequent eddies and filaments on the GS lateral boundaries (Glenn and Ebbesmeyer 1994; Brooks and Bane 1983) and the diffuse nature of the GS eastern edge. The GS position exhibits a strong dependence on edge definition (Richardson 1985; Halkin and Rossby 1985). For example, the GS edge has historically been defined by characterizing satellite infrared imagery of SST gradients (Miller 1994; <https://polar.ncep.noaa.gov/global/monitor/>), by a preestablished isotach (Halkin and Rossby 1985), sea surface elevation (Kelly 1991; Kelly and Watts 1994), by isotherms (Fuglister 1951), or isohalines (Richardson 1985), and SSH (Gula et al. 2015).

Previous efforts to compare and evaluate the efficacy of both direction-finding (DF) and beam-forming (BF) radars in this region was undertaken by Shay et al. (2008). Archer et al. (2017) used BF radars to study the surface velocity structure of the GS in the Florida Straits and compared the kinematic similarity with that of the East Australian Current (Archer et al. 2018). This is the first study to measure the GS properties off Cape Hatteras with DF radars.

b. HF radars

Land based HFRs provide higher temporal resolution of the GS than historical methods. A single, monostatic, 5-MHz HFR measures the radial component of the ocean surface current field at an array of locations relative to the receive antenna in the water column's top 2–3 m, herein called radials. The “surface” depth depends on the wavelength of the radar (Barrick et al. 1977). This depth is approximately $\lambda/8\pi$, where λ is the radar wavelength, or about 2.7 m for the 5-MHz North Carolina radars being used herein (Paduan and Graber 1997). Radial current measurements from the systems used in this study are produced every hour. Typical processing for CODAR Ocean Sensors 5-MHz HFRs produce radial velocity maps every 30 min, which are then averaged over a 2 h 30 min window, with the azimuthal resolution decreasing as a function of range from the radar, that form a repeating tessellation of cells. Each vector is a spatial average over an annulus bounded by a 5.85-km range difference, and 5° bearing separation. The HFR range coverage varies from about 100 to 200 km due to environmental influences like variations in the ocean surface wave field necessary for signal reflection, nighttime ionospheric interference that tends to limit range (Menelle et al. 2008), and interference from external noise near the radar frequency band (Emery et al. 2004).

In this study we have chosen to work with radial current measurements, rather than the full vector current field produced by the combination of radial velocities from two or more sites. The primary reasons for using radial rather than total velocities are the more consistent and greater spatial coverage available from the radial vectors (Bourg and Molcard 2021). Figure 2 demonstrates the difference in spatial coverage, as percent coverage for the month presented below, for the HFR sites along the North Carolina coastline. Of particular note is the greater offshore extent of the radial coverage compared to that of the totals. Another advantage to using only radial velocities for this method is the elimination of uncertainty introduced by the geometric dilution of precision from combining radials into total velocities. Our decision to pursue a method applied to the radials is pragmatic, with the aim to maximize valid representations of the GS over time and over the space it occupies.

2. Methods

A method to extract characteristics of the GS surface flow field is applied to observations from two HFRs located on the North Carolina coast that consistently measure surface currents in the GS. HFRs in the Integrated Ocean Observing System (IOOS) are given four letter identifiers: HATY is located in Buxton, North Carolina, on the north side of Cape Hatteras (Fig. 1a), and CORE on the Core Banks of North Carolina north of Cape Lookout at the National Park Service's Great Island Campground (Fig. 1b). The month of November 2014, when both radars operated the majority of the month, was selected for analysis and algorithm development. HATY has been operating since 2003 (Shay et al. 2008), and CORE was added in 2013.

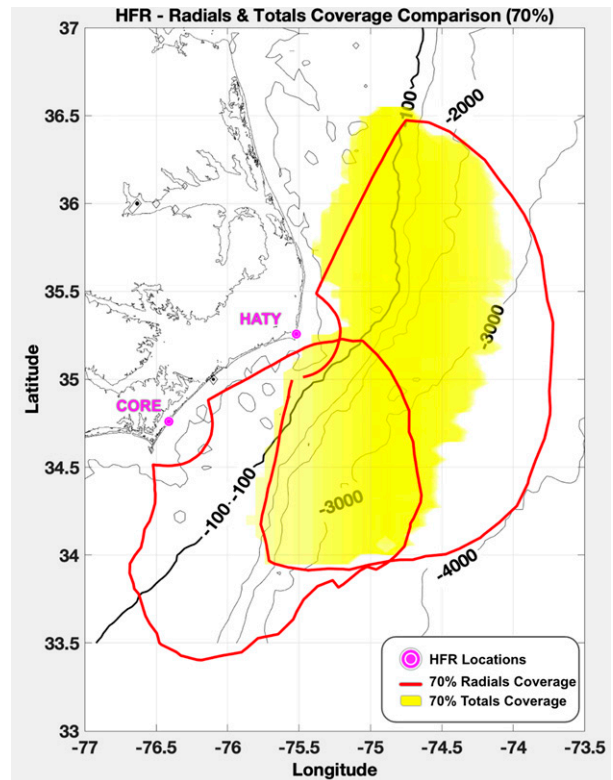


FIG. 2. The 70% coverage zones (red contours) for radials from HATY and CORE and for radial-combined total surface currents (yellow shading) during November 2014.

The radial components of the surface currents measured by the radars have known quality control considerations that are specific to each site (Liu et al. 2010). A recent effort to improve the quality of the radial surface currents for the sites in this study (Haines et al. 2017) implements the processing advocated by Kirincich et al. (2012), with some modifications. The method uses signal and solution quality nonvelocity metrics provided for DF radar systems to eliminate low-quality radial velocity solutions in hourly radial output files. The process reduces uncertainty over the entire footprint and demonstrates that the radar uncertainties increase with distance from the radar. In comparisons between four months of ADCP and HFR radial currents the method reduced the standard deviation of residuals on the shelf from 9 to 8 cm s^{-1} and from 16 to 13 cm s^{-1} and over the slope from 17 to 15 cm s^{-1} and 57 to 46 cm s^{-1} for HATY and CORE radars, respectively. The large errors in the CORE HFR comparisons on the slope are caused by the significantly greater distance from the HFR to the ADCP. The quality control method reduces a low velocity bias in radar currents in the GS by 15%–20% (Haines et al. 2017). The method presented uses these quality-controlled radar radial currents.

The monthly mean radial speeds for this study from the HATY and CORE HFRs are shown in Fig. 1. By convention, radial speeds toward the radars are negative, and those away are positive. The cooler colors south of HATY where averaged radial speeds are most negative are those where the GS enters

the radar coverage, and the hot colors with large positive magnitudes are indicative of the GS exiting to the northeast. The GS is not apparent in radial surface current measurements when its surface current direction is perpendicular to the radar radials. The location of the GS landward edge and jet axis are apparent in the monthly averaged radial speeds as the largest landward gradients and radial maxima/minima, respectively. Further, a metric of the width of the GS CSZ, a distinct area in the GS with positive relative vorticity (Archer et al. 2018), is defined to be the distance between the maximum velocity gradients and maximum radial velocities. The metric is approximately the half-width of the CSZ when the full width is defined to be the distance from the GS 20 cm s^{-1} inshore isotach to the jet axis (Fig. 3).

The following method identifies the distance from the radar site to the maximum (minimum) radial gradient and maximum (minimum) radial velocity. These values are then used for determining a measure of the CSZ width and the orientation of the GS. The following data preparation and analysis steps detail the method.

a. Step 1: Elimination of (i) poor coverage areas and (ii) hourly radial files with insufficient data

Consistent spatial coverage throughout the study period is necessary to establish GS position; hence, a first step is to identify the minimum coverage required. While thresholds for data coverage defined by the number of radial solutions are site specific and reliant on local environmental factors that affect site performance, generalized application of this method is possible for any monostatic HF radar. Radar measurement cells where radials were not observed with at least 30% consistency over the month were eliminated from further analysis (Fig. 1). Imposing a threshold greater than 30% on the consistency removed measurements to the detriment of the algorithm.

Additionally, a site-specific number of cells with radial velocity measurements was required for each hourly radial file to be included in analysis: 47% of the average number of hourly solutions for HATY and 60% for CORE. The number of required cells with radials for each radar was chosen by visually examining each radar's hourly radial coverage for the month, and requiring each radial file to have enough solutions to provide radials from near the installation to offshore of the maximum values indicative of the GS jet axis. The average number of cells is ~ 1500 for HATY and ~ 750 for CORE, and the maximum number of cells is 2500 for either radar. The greater distance to the GS from CORE means a higher percentage of solutions is required for the algorithm to be effective. Bearings without radial velocities at more than half of the ranges over the monthly time series were eliminated from analysis.

b. Step 2: Radar bearing selection for analysis

Four bearings from each radar where GS currents were consistently measured over the month were selected for analysis (Fig. 1). Bearings were selected from within the region of most negative (positive) radial velocities where the GS enters (exits) the radar coverage to focus method application where GS presence is most consistent. To choose bearings for analysis,

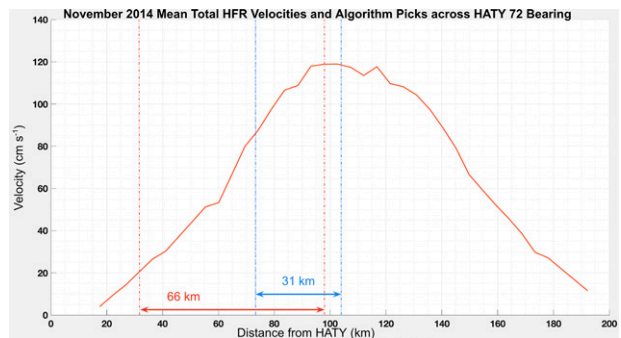


FIG. 3. An examination of the CSZ along the HATY 72° bearing. The month-averaged algorithm GS edge and jet selections (blue) are compared to the month-averaged surface current speed derived from the HFR total vector field along the HATY 72° bearing. Red vertical lines mark the landward 20 cm s^{-1} isotach and maximum speed.

radial velocities were averaged along each azimuth over all ranges every hour. The least (greatest) averaged radial velocity magnitudes were selected each hour, and the bearing of the mode hourly minimum (maximum) current magnitudes over the time series were chosen for analysis. We refer to these as “mode bearings.” Bearings at the shoreward edges of the radars’ coverage were not considered because the majority of the radials were on the shelf. Thus, some mode-bearing selections were nudged 5° – 10° offshore to avoid selecting bearings that were on the edge of coverage. Thereafter, two additional bearings were added 15° seaward of the initial two bearings, referred to as “proximal bearings” (Fig. 1). They provide additional edge and jet axis position information, and an estimate of GS orientation between the mode bearing and the proximal bearing 15° seaward. Thus, the method focuses inspection on regions where the GS has the strongest current signal in the radial coverage over the sampling period, without analyzing azimuths on the edge of radar coverage.

c. Step 3: Zero filling and radial smoothing

Radial velocities along the chosen azimuths are typically noisy and can have numerous missing values (Figs. 4a,c). Simple interpolation led to errant values for some missing values. As an alternative approach zero filling was used to infill missing radial values, prior to smoothing using a 4×4 convolution in space and time – 17.4 km and 3 h, respectively. The convolution was chosen for mitigating noisy data; smaller convolution windows were not as effective, larger windows did not capture higher-frequency meander variability. Zero filling was found to enhance GS edge selection at gradient maxima (Figs. 4b,d), though it may lead to an underestimate of velocities seaward of the jet axis. Hourly radials that did not meet the criterion for sufficient number of solutions were eliminated from further consideration (gaps in coverage Fig. 4).

d. Step 4: Gulf Stream edge and jet detection, and cyclonic shear zone width

The GS jet axis along a selected bearing was assumed to be at the smallest (largest) radial velocity where the GS enters (exits)

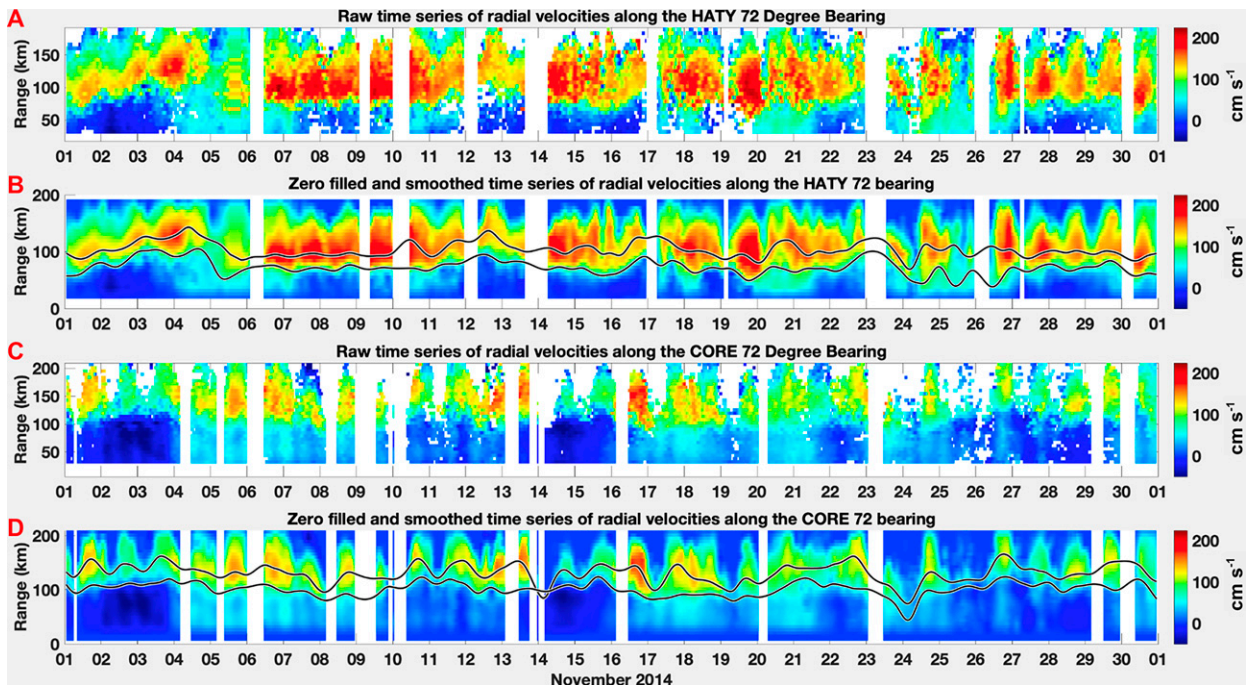


FIG. 4. (a) Raw radial speeds along the HATY 72° bearing and (b) zero-filled and smoothed radial speeds. Also shown in (b) are edge (lesser range) and jet axis (greater range) distances from the radars after cubic spline smoothing. (c) Raw radial speeds along the CORE 72° bearing, and (d) zero-filled and smoothed radial speeds with the method selection for the edge (lesser range) and jet axis (greater range) distances after cubic spline smoothing. Time periods where an insufficient number of radial solutions are available for analysis have been eliminated.

radar coverage. The GS's landward edge along the bearing was then assumed to be the location of the largest difference between radial velocity estimates in the radial direction inshore of the jet. Edge and jet axis selections were required to be at least 23.4 km from HATY and 35.1 km for CORE, or offshore of the third and fifth range cells for each radar (the first range cell is blanked). This requirement eliminated the contamination of edge selections that infrequently occurred on the shelf from extreme shelf currents that were well onshore of the shelfbreak.

The ranges from each radar to the position estimates occasionally suffer from rapid shifts that are clearly unphysical. To mitigate this, a filter was applied to remove estimates where the edge and jet axis position changed by more than 13 km, or more than two range cells, in an hour. The hourly GS edge and jet axis time series were then smoothed using a cubic spline that applies a 24-h low-pass filter.

The distances between GS edge and jet axis locations are our metric of the cyclonic shear zone width and location. This distance is approximately half the distance from the jet axis to the shoreward GS edge (Fig. 3).

e. Step 5: Gulf Stream orientation

GS edge and jet axis detection locations along mode bearings and those along the proximal bearings were connected to provide a GS orientation estimate (Fig. 6), assumed to be the angle of the line that joins edge or jet axis selections. Thus, four orientation estimates are made from each radar every hour, two edge orientation and two jet axis orientation estimates.

Using these steps, smoothed hourly estimates of GS edge and jet axis position and CSZ width metrics are produced for each one of the four radial bearings at each site. Additionally, for each mode- and proximal-bearing pair an edge and jet axis orientation estimate is produced as well. The crossing angle of radar bearing relative to the GS orientation influences the quality of the estimates. The influence of the GS's orientation on the radar-derived estimates is represented schematically in Fig. 5. In Fig. 5a, the GS is oriented perpendicular to the radar bearing. In this case, GS flow is orthogonal to the radar radial

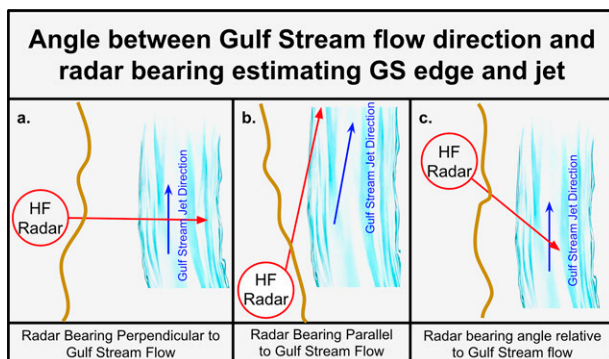


FIG. 5. Three different examples of HF radar bearing relative to the GS flow. (a) The GS is perpendicular to the radar bearing, and no GS estimates are possible. (b) The GS is nearly parallel to the radar bearing, and accurate estimates of the jet are not available. (c) The radar bearing is at an angle of about 45° with respect to the GS flow, the optimal case for the method.

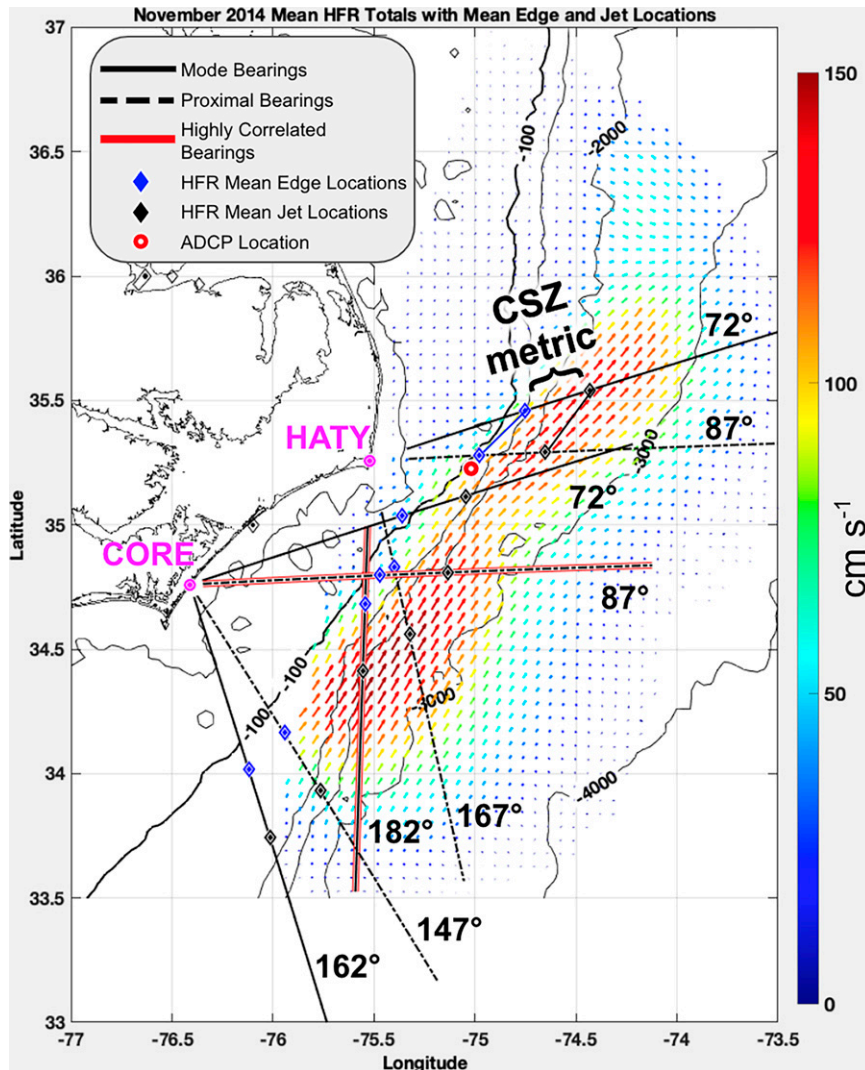


FIG. 6. The average HFR-derived total velocity field, overlain on a map of the North Carolina coastline and isobaths (m), ADCP mooring location (red), HATY and CORE radar locations (pink), mode (solid line) and proximal (dashed line) bearings selected by the method for GS measurements for the month of November 2014. Blue diamonds represent mean edge estimates along the bearings, and the thin blue line connecting the edge estimates between the HATY 72° and 87° bearings is the associated GS orientation. The black diamonds are mean jet axis estimates; the thin black line drawn between them is the associated orientation estimate. The red bearings are the most correlated mode bearings between the two HFR sites.

and there is zero contribution to the radial velocities along that bearing from the GS. There is no detectable signal from the GS. No estimates of GS edge, jet axis, or orientation are possible for this instance. In Fig. 5b, the GS jet and radar bearing are nearly parallel. The radar range to the jet axis may be undetermined. Theoretically, as bearing and orientation become parallel, range is infinite. In reality, the estimate will be made at the location of the highest radial velocity within the radar range limits, not necessarily at the GS jet axis. The radar may still choose the edge of the GS accurately in this instance. The algorithm is optimal for Fig. 5c, where the angle between bearing and GS orientation

produces significant radial velocities and range from the radar to the edge and the jet axis are located within the radar coverage range. The algorithm is designed to maximize the instances of the latter case, Fig. 5c, by focusing analysis on bearings most often oriented like this relative to the radar.

3. Results

a. Measurements

Hourly estimates of the range from HATY and CORE to the GS edge and jet axis were made for the eight bearings selected

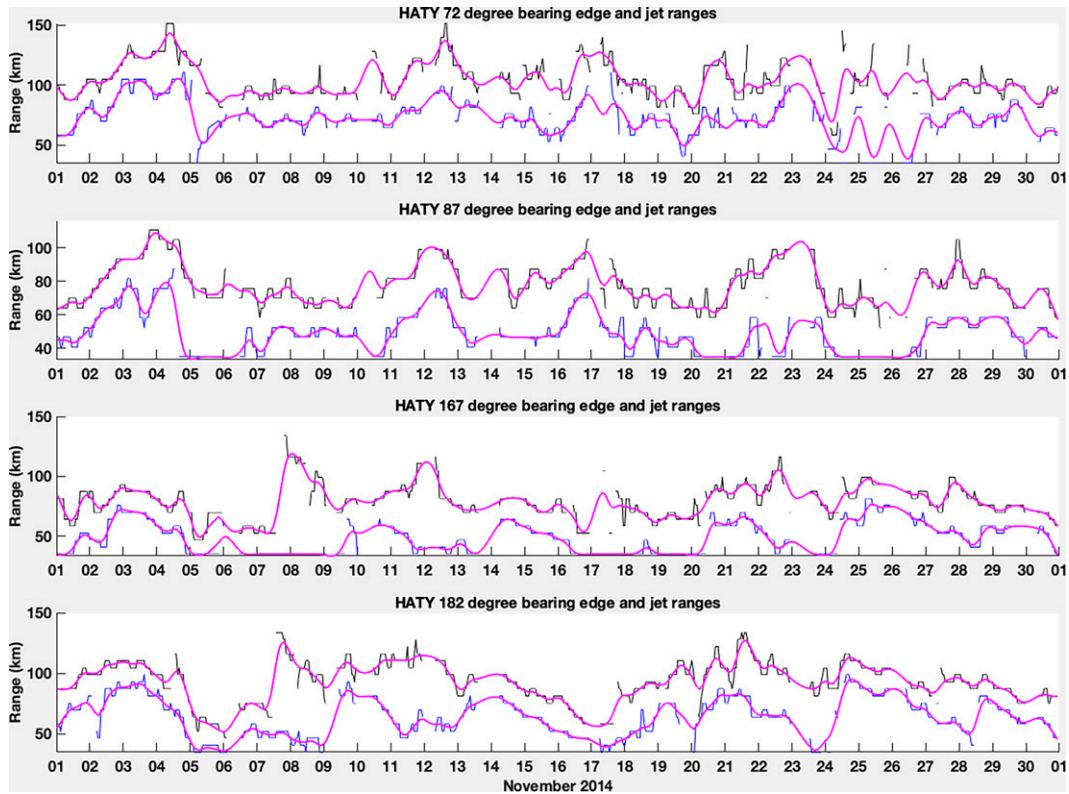


FIG. 7. Hourly values of the range from the radar to the edge (blue) and jet axis (black) for all four HATY bearings overlaid with 24-h low-pass cubic spline (magenta).

by the algorithm: four from each radar. Mode bearings selected were 72° and 182° from HATY, and 72° and 162° from CORE, paired with proximal bearings 87° and 167° for HATY and 87° and 147° for CORE, respectively. GS edge (blue) and jet axis (black) selections along paired mode and proximal bearings are connected, shown in Fig. 6 for the HATY 72° and 87° bearings, to provide an estimate of the GS edge and jet orientations.

Examples of the raw and smoothed hourly radial data for HATY and CORE 72° mode bearings are given in Fig. 4. The figure also displays the cubic spline fits of the edge (inshore) and jet axis (offshore) selections and visually demonstrates how the algorithm method selects the GS edge and jet axis ranges from the radars based on velocity gradients and minima/maxima, respectively. A notable difference between the observations from the two radars depicted in Fig. 4 is the greater range from the radar to the GS along the CORE 72° bearing, and the lower data quality that results from estimates made farther offshore to be inshore of the edge. The lower signal to noise values at the greater ranges along this bearing do not provide edge and jet axis estimates of high-enough quality to provide confidence in the monthly mean locations of both.

In Figs. 7 and 8, the blue and black curves are the hourly estimates of the distance from the HATY and CORE radars to the GS edge and jet axis, respectively, along each of the eight radar bearings. The magenta cubic spline fits reduce noise and fill data gaps, providing reasonable estimates of the edge and jet locations over the month most of the time.

Time scales for variability in GS position are 2–14 days for all of the bearings. The range from the radars to the GS varies by about 50 km along HATY bearings, and by about 75 km for CORE. The edge and jet axis estimates often track each other for each bearing, with three to five exceptions during the month. Some of the exceptions may be caused by physical differences in the orientation of the GS edge and jet axis relative to a radar bearing.

1) HATY

For brevity, detailed descriptions are presented only for the northern bearing selections from each radar. Examining the results of the 72° and 87° HATY bearings first provides a good foundation for comparing the 72° and 87° CORE bearings later, because the GS is closer to HATY and as a result the closer edge and jet axis are better sampled.

Changes in HATY edge and jet axis ranges clearly covary along the 72° and 87° bearings. The covariance is apparent over the entire sampling period. The correlation coefficient for the variability in edge ranges between the two bearings is 0.66, with the 87° bearing leading the 72° bearing by five hours. Typical ranges to the edge from 72° bearing are ~ 50 km and vary from about 20–90 km, while jet ranges are ~ 100 km varying from 60 to 140 km (Fig. 7).

Simultaneously examining the relationships between radar estimates of GS range and radial velocity at each edge and jet axis selection provides insights about the method (Figs. 9a,b

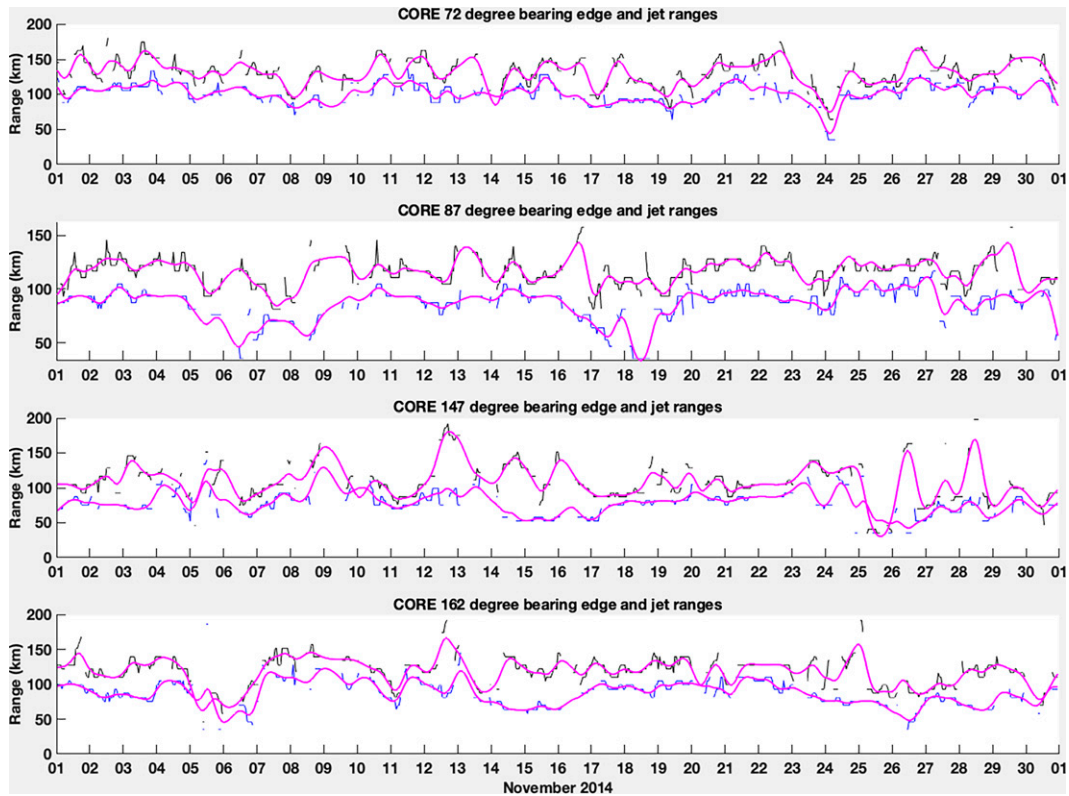


FIG. 8. Hourly values of the range from the radar to the edge (blue) and jet axis (black), for all four CORE bearings overlaid 24-h low-pass cubic spline (magenta).

and 10a,b). Radial velocities are $1\text{--}2\text{ m s}^{-1}$ in the jet axis and less than 1 m s^{-1} at the edge; it is not obvious how variations in speed relate to variations in position, but one expects the radial speeds to be indicative of the large GS speeds as the figures demonstrate. If the radial speeds at edge and jet estimates (Figs. 9b and 10b) are lower than those expected in the GS, the confidence in the accuracy of those range estimates is reduced. This is less of a concern for HATY than for CORE but is most pronounced along the HATY 87° bearing (Fig. 10b) on 16 November and less so between 22–23 and 28–29 November.

In conjunction with the radial speeds and range estimates, it is also important to consider the radar bearing relative to the orientation of the GS (Figs. 9c and 10c). The relative orientation can affect the radial velocities, since only a component of the GS velocity is measured by the radar. Red lines in Figs. 9c and 10c identify the radar bearing along which GS estimates are made, and the direction orthogonal to the bearing. When the GS orientation approaches the radar bearing, distance estimates to the jet theoretically approach infinity, and realistically become inaccurate. If the orientation approaches a direction that is orthogonal to the radar bearing, edge and jet ranges, as well as orientation estimates, increase in uncertainty since GS velocities approach zero. The HATY bearings presented do not suffer from these occurrences. They are most pronounced on the CORE radar and are discussed in the next section.

The difference between the distance to the edge and jet axis is a measure of the CSZ width (Figs. 9d and 10d). Variability in the

radar estimates of the CSZ width could be due to variability in GS structure along a bearing over the time series or caused by changes in GS orientation relative to the radar bearing. As a possible example of the latter, we note the difference in CSZ width that occurs between 21 and 24 November along the HATY 72° and HATY 87° bearings (Figs. 9d and 10d). During this time, CSZ width is $\sim 20\text{ km}$ along the 72° bearing and $\sim 55\text{ km}$ along the 87° bearing. The width along the HATY 72° bearing is fairly steady for that time period, while the HATY 87° bearing width changes by about 35 km. Both bearings exhibit pronounced changes in distance estimates to the GS edge and jet axis during those days (Figs. 9a and 10a) indicative of meander propagation. Also, the edge and jet axis orientation estimates (Figs. 9c and 10c) from pairing both bearings are consistently offset more than any other time during the month. Physically, this could also be the result of making those estimates at different locations within a meander. The meander orientation relative to the 87° bearing is the probable cause of the wide range of CSZ widths along that bearing.

2) CORE

Overlooking some of the obvious errors in the range estimates (Fig. 8) caused by data omissions and periods of noisy data at CORE, the temporal and spatial scales of variability agree with expectations for this region. Ranges to GS edge and jet axis are further offshore than those from HATY, in

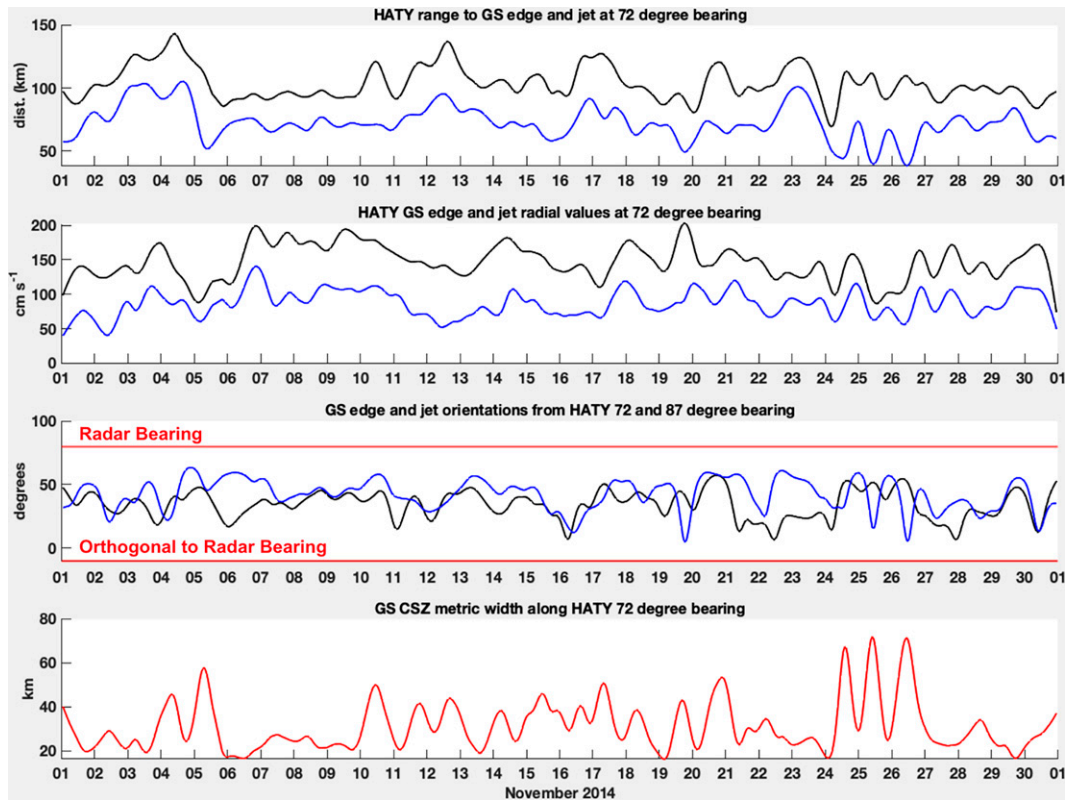


FIG. 9. (a) HATY 72° bearing estimates of edge and jet axis ranges, (b) radial velocities at the edge (blue) and jet axis (black) selections, (c) GS edge (blue) and jet axis (black) orientation estimates between HATY 72° and HATY 87° with red horizontal lines showing the radar bearing and bearing orthogonal to it, and (d) the CSZ width defined as the distance between the edge and jet estimates. All curves are cubic spline fits.

agreement with the mean GS path south of Cape Hatteras as determined in prior studies (e.g., Miller 1994). CORE ranges vary more than HATY, especially along the southern CORE bearings. Edge and jet axis ranges vary by ~ 50 km with maximum shifts of ~ 100 km. Meander time scales evident in the radar ranges are 2–14 days. Most of the variability seen in the edge position is also seen in the jet axis estimates, with several notable exceptions caused by radar noise or data omission: 14 November on bearing 72°, 18 November on bearing 87°, and 12–17 and 23–27 November on bearing 147°.

The noisier estimates from CORE relative to those from HATY are the result of lower radar signal to noise levels at greater ranges, which manifests as occasional low radial speeds along the CORE 72° bearing (Fig. 11), and in noisier range estimates along all CORE bearings (e.g., compare Figs. 7 and 8). The greater range estimates from CORE often approach the limits of the radar coverage, increasing their uncertainty (Haines et al. 2017). Because jet axis estimates are the most distant from the radar, the estimates of jet axis location and jet axis orientation can be expected to be of lower quality and higher uncertainty than those for the edge.

As with HATY, it is informative to consider the method's performance for the chosen bearings by examining edge and jet ranges with radial velocities at those picks, GS orientation relative to the radar bearing, and CSZ width (Fig. 11).

Examining the CORE 72° bearing, the best data quality is from 1 to 4 November, while more noise and omissions occur during 5–10 and 21–24 November. The variability in the ranges to the edge and jet axis track each other well, and the distance between them is quite consistent with a few exceptions. One notable exception occurs on 14 November when the jet axis estimate is inshore of the edge. This is an outcome of the cubic spline fit to the jet range estimates trending toward lesser ranges before radial data become too poor to be included, continuing the fit trend inshore until data become available again (Fig. 4d). Similarly, the jet axis and edge orientation estimates from the 72°/87° bearings (Fig. 11c) are largely consistent up until the 14 November. Range variability seen on the CORE 72° bearing from 22 through 25 November appears to capture a GS meander also seen on the CORE 87° bearing to a lesser extent (Fig. 8). The more prominent signature of the edge and jet axis ranges along the 72° bearing could be caused by the difference in GS crossing angle with respect to both bearings. The radial velocities at the jet axis fluctuate around 100 cm s^{-1} , and at the edge about 50 cm s^{-1} (Fig. 11b). Notable are the lesser CSZ width estimates from the CORE 72°/87° bearings when the GS orientation is nearly orthogonal to mode bearings on 8, 10, 14, 19–21, and 24–26 November (Fig. 11d).

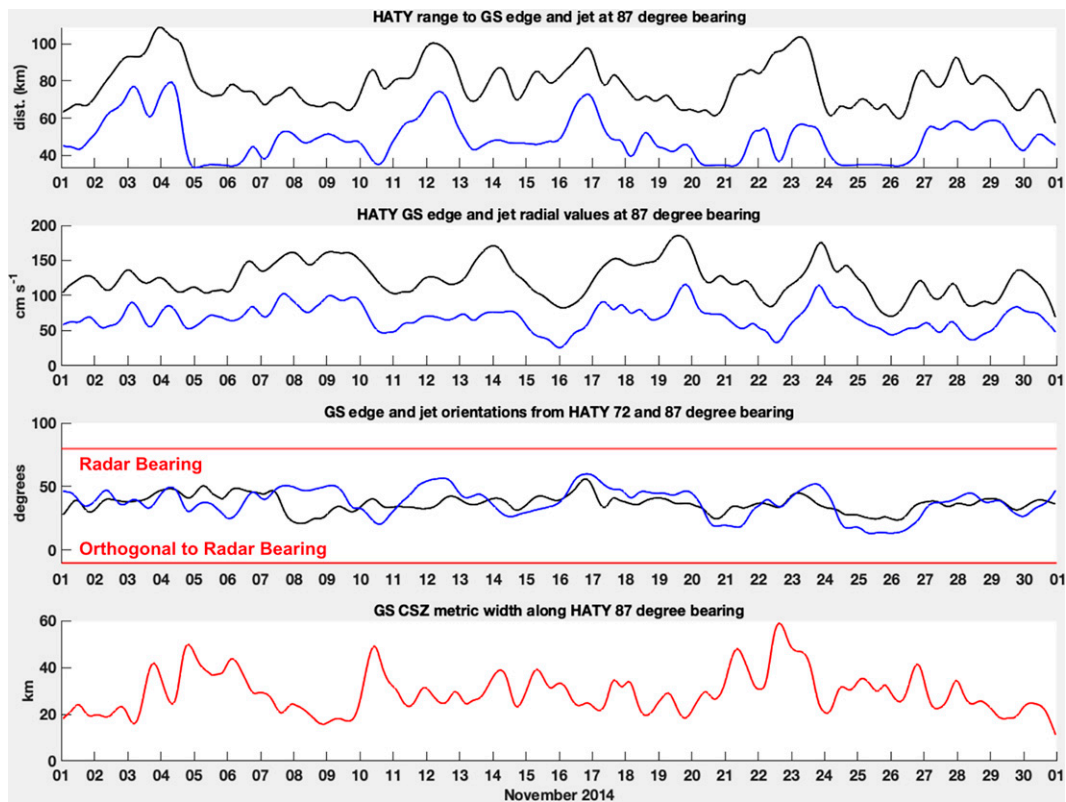


FIG. 10. (a) HATY 87° bearing estimates of edge and jet axis ranges, (b) radial velocities at the edge (blue) and jet axis (black) selections, (c) GS edge (blue) and jet axis (black) orientation estimates HATY 72° and HATY 87° with red horizontal lines showing the radar bearing and bearing orthogonal to it, and (d) the CSZ width defined as the distance between the edge and jet axis estimates. All curves are cubic spline fits.

Near-zero edge radial velocities on 14–15 November do not reflect what is expected where the maximum gradient is chosen to be the GS edge. They correspond with an edge GS orientation estimate that approached orthogonality with the 72° bearing, and a range estimate to the jet that is less than that to the edge. The cause is apparent in Fig. 4d, when there is a sustained absence of radial velocities during 13–14 November.

3) MONTHLY AVERAGE GS PROPERTIES

In addition to evaluating radar performance for individual bearing parameter time series, it is informative to examine the means of the parameters over November 2014 to assess if measurements being made are physically realistic. Despite noisy periods in each parameter time series, if monthly means are consistent with known GS parameters in this region it provides confidence in overall method performance. Monthly mean estimates of edge and jet axis distance from the radars and from the 100-m isobath, cyclonic shear zone width, maximum (minimum) radial speeds, and orientation are shown in Table 1. Values in the table are derived from the continuous cubic spline curves.

There are notable differences in distance estimates from each radar. The mean ranges to the GS edge and jet axis presented in the table are displayed on each bearing in Fig. 6.

The map provides perspective between relative radar locations, estimates, and the underlying bathymetry. The edge and jet axis mean locations are seaward of the 100-m isobath, with one exception. Mean edge locations are farther offshore of the 100-m isobath to the south and move progressively closer to the 100-m isobath as the Point is approached; this is consistent with previous depictions of the GS path along the North Carolina coast (e.g., Miller 1994). From Table 1, the GS is most distant from the radar installation along the CORE 72° and 162° bearings, and as mentioned previously, the range of all CORE estimates are greater than those from HATY. The mean edge estimate for CORE 72° is notably landward of the 100-m isobath (Fig. 6), a likely cause being the increase in uncertainty caused by the distance of these estimates. The corresponding jet axis mean location along the same bearing is also the most shoreward of the jet axis means. The mean orientation estimates from the paired CORE 72°/87° bearings are much different than the other paired bearing means as well.

Despite large short-term variability in CSZ width estimates along individual radar bearings discussed previously, the mean widths seen in Table 1 for all eight radar bearings are quite consistent. The range of mean CSZ width for all bearings is only 3 km.

All means are valuable for method comparison with values found in the literature and will be discussed further below.

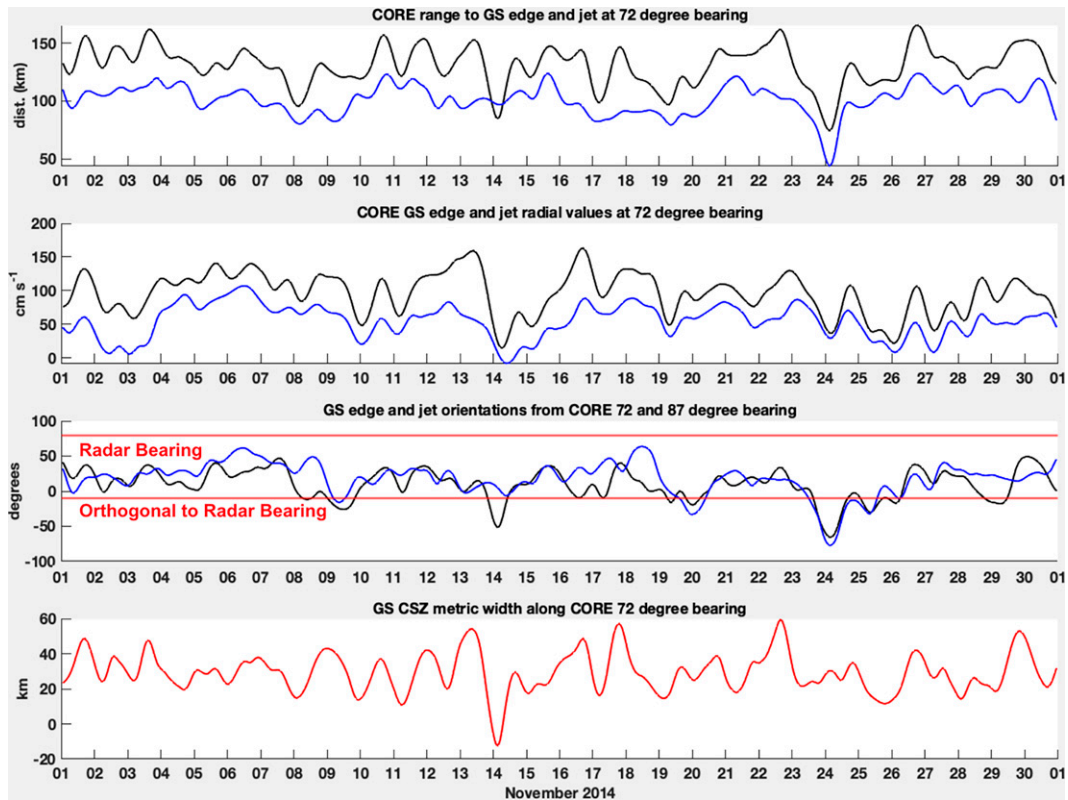


FIG. 11. (a) CORE 72° bearing estimates of edge and jet axis ranges, (b) radial velocities at the edge (blue) and jet axis (black) selections, (c) GS edge (blue) and jet axis (black) orientation estimates CORE 72° and CORE 87° with red horizontal lines showing the radar bearing and bearing orthogonal to it, and (d) the CSZ width defined as the distance between the edge and jet axis estimates. All curves are cubic spline fits.

b. Method evaluation

Three different independent comparisons are presented to establish the efficacy of the method. The first compares the mean GS edge and jet axis locations from the algorithm with the mean SSH and SSTs during November 2014. The second compares independent measurements of the landward GS edge location, orientation, and CSZ width between CORE and HATY along crossing and parallel bearings. The third examines the relationship between radar GS edge estimates and the current velocities over the water column from a collocated acoustic Doppler current profiler (ADCP) mooring in the radar footprint during November 2014.

1) MONTHLY MEAN COMPARISONS WITH SSH AND SST

To assess consistency with fully independent measurements, the monthly mean HFR estimates of the GS edge and jet axis position are compared to the monthly averaged SST and SSH (Fig. 12). The NOAA Coastwatch SST monthly composite and monthly averaged absolute dynamic topography, derived from the daily gridded $1/4^\circ$ SSH product from Copernicus Marine Environmental Monitoring Service are used. The HFR jet axis estimates lie on or just offshore of the 0.4-m SSH contour, consistent with Zeng and He (2016), who examined Gulf Stream position upstream of Cape Hatteras in

21 years of SSH data. The edge estimates are near the 0.25-m contour. The consistency of the HFR position estimates with the SSH fields is encouraging. The shoreward-shifted CORE 72° bearing estimates are the exception, the higher uncertainty likely caused by the greater distance from the radar to these estimates. There is limited structure to the monthly averaged SST image with which to make a quantitative comparison.

2) CORE AND HATY INDEPENDENT MEASUREMENT COMPARISONS

Comparisons were made for several bearing combinations between HATY and CORE. Each radar provides independent estimates of range from the radars to the edge, jet axis, and GS orientation. Comparisons between different radars begin to characterize the accuracy and skill of the algorithm. This intercomparison is useful because it compares independent measurements of the same parameters with the same temporal resolution and similar spatial resolution.

Comparisons focus on either bearing estimates that overlap or estimates from parallel bearings from each radar. Lagged correlations between bearings were stronger at GS edge estimates than jet axis estimates; thus, edge measurement comparisons are presented (Table 2). It is likely that the greater range of the jet axis estimates, with lower signal to noise ratios, is responsible for the

TABLE 1. Mean values for all CORE and HATY analysis bearings, including edge and jet axis distances from each radar/from the 100-m isobath (top two values in columns 2 and 3) and water depth (bottom value) at the estimates. CSZ metric width, radial speeds at edge and jet axis selections, and paired orientation estimates from both the edge and jet ranges.

Bearing	GS edge distance (km) and depth (m)	GS jet axis distance (km) and depth (m)	CSZ width (km)	Edge radial speed (cm s ⁻¹)	Jet radial speed (cm s ⁻¹)	GS orientation edge (°)	GS orientation jet (°)
HATY 72°	73/10 815	104/40 2441	31	87	147	38	32
HATY 87°	49/2 252	78/30 2414	29	68	124		
HATY 167°	48/14 349	79/45 2566	31	-47	-93	45	54
HATY 182°	64/16 325	94/46 2241	30	-63	-120		
CORE 72°	101/-6 66	131/24 728	30	55	96	16	9
CORE 87°	86/8 258	117/39 2363	31	47	84		
CORE 147°	79/13 362	109/44 1323	30	-23	-44	44	44
CORE 162°	87/13 339	118/44 690	31	-32	-67		

lower correlations. All p values for correlations were less than 0.05, and thus have statistical significance at the 95% level or higher (Taylor 1997). Correlation coefficients for daily averaged values of the ranges were also evaluated to assure that correlations had a statistical significance greater than 95% despite the 24-h low-pass filter applied to reduce noise.

The strongest correlations were between edge measurements from the individual radars that are nearly collocated, and from adjacent bearings. Correlation coefficients less than ~0.50 were found to produce physically unrealistic lags. Correlations between orientation estimates were evaluated, but all were 0.40 or less and are not included in the table.

Ranges from each radar to the GS edge estimates along the HATY 182° and CORE 87° bearings (see Fig. 6) had the strongest correlations at 0.73 with CORE 87° lagging HATY 182° by seven hours (Table 2). Ranges along the HATY 167° and CORE 72° bearings were nearly as well correlated and have the same lag. HATY edge selections are typically upstream of CORE selections; thus, the lag between these bearings appears physically sound. Range correlation along the HATY 167° and CORE 87° bearings is 0.66 with zero lag. The two bearing estimates are nearly collocated (Fig. 6). These significant correlations between several collocated measurements and radial velocities, with lags that are physically reasonable, lend credence to the method accuracy.

Lags for less correlated parallel bearings from each radar like HATY and CORE 72° and 87° bearings are reasonable, with upstream estimates leading downstream as expected for meander propagation in this region. The less well-correlated radial velocities have similar lags. Only the CORE 147° bearing estimate that lags the HATY 182° bearing appear inconsistent, with a much more extreme lag time of about 9 days.

3) HATY/CORE 72° AND 87° COMPARISONS WITH COLLOCATED ADCP

A Teledyne RDI 150-kHz Sentinel ADCP was moored just south of the HATY 87° bearing and just north of the CORE 72° bearing during November 2014. The mooring was maintained on the upper slope east of Cape Hatteras at ~35.19°N, 75.06°W in a water depth of 260 m (Fig. 6). The ADCP measured currents with 4-m vertical resolution over most of the water column every 10 min—excluding only the bottom ~8 m and top ~28 m. The 10-min measurements were hourly averaged. The ADCP currents were rotated into a streamwise coordinate system with the downstream direction defined to be the depth and time averaged direction over the entire monthly record—northeast at 40° in this case. The positive cross-stream direction is nearly cross isobath offshore.

The frequent GS meander crests and troughs that propagate through the region during the month appear in both the downstream ADCP current observations and GS edge estimates from the method. Despite the differences in spatial and temporal resolution of both instruments and the differences in measurement depth in the water column from each, a clear relationship appears between the higher currents indicative of the presence of GS meander crests over the ADCP and reduced ranges to the GS edge along the radar bearings (Fig. 13, red rectangles). Similarly, the greater distance to the GS edge along the radar bearings occurs when downstream current velocities at the ADCP decrease in the presence of GS meander troughs (Fig. 13, blue rectangles).

Four specific examples of meander trough/crest propagation through the region are highlighted in Fig. 13 and discussed herein. On 5 November, the distance from the CORE radar to the GS edge along the 87° bearing declines from ~90 to 60 km. The event lasts 5 or 6 days on both the CORE 87° and 72°

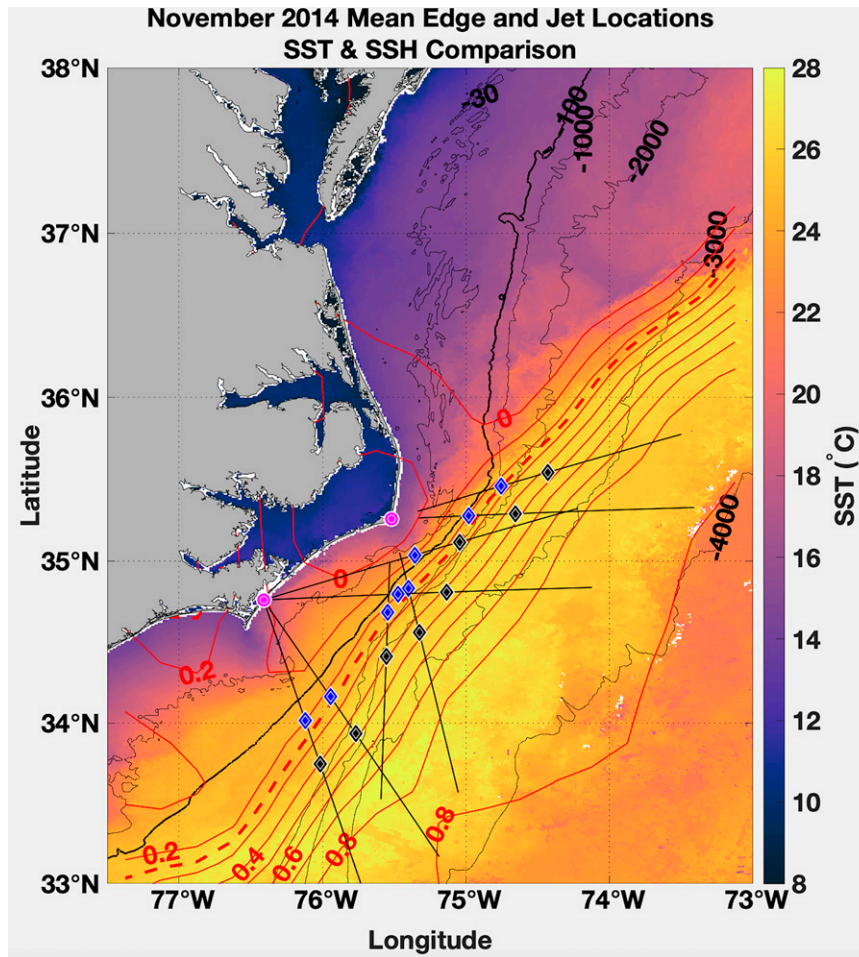


FIG. 12. November 2014 mean edge (blue diamonds) and jet (black diamonds) locations determined by the method overlaid on the month-averaged SST (shown as a heatmap) and month-averaged SSH contours. Edge locations align with the 0.25-m SSH contour and jet axis locations with the 0.4-m SSH contour.

bearings (Fig. 13, bottom two panels). The downstream currents measured by the ADCP begin to increase and deepen from 5 through 11 November (Fig. 13, middle panel), characteristic of GS meander crest structure (Bane et al. 1981). The passage of the crest, marked as red rectangles, is seen at the mooring as the deepest penetration of high currents, and as a decrease in

distance to the GS edge propagating past the HATY 87° and 72° bearings. Immediately following the passage of that crest, on 10 and 11 November, a meander trough causes an increase in distance to the GS edge along the CORE 87° and 72° bearings and is accompanied soon after by a reduction in downstream velocities throughout the water column at the ADCP

TABLE 2. Correlations for hourly (daily) range values and lags for hourly range values at GS edge between pairs of HATY and CORE select bearings.

Bearing pair–edge	Cross correlation coefficient edge ranges	Lag
HATY 72°–HATY 87°	0.66 (0.72)	5 h: HATY 72° lags HATY 87°
HATY 72°–CORE 72°	0.45 (0.61)	32 h: HATY 72° lags CORE 72°
HATY 87°–CORE 87°	0.37 (0.44)	46 h: HATY 87° lags CORE 87°
HATY 87°–CORE 72°	0.49 (0.66)	27 h: HATY 87° lags CORE 72°
HATY 167°–CORE 72°	0.70 (0.47)	7 h: CORE 72° lags HATY 167°
HATY 182°–CORE 72°	0.57 (0.70)	14 h: CORE 72° lags HATY 182°
HATY 167°–CORE 87°	0.66 (0.72)	0 h
HATY 182°–CORE 87°	0.73 (0.62)	7 h: CORE 87° lags HATY 182°
HATY 182°–CORE 147°	0.65 (0.62)	220 h (9.17 days): CORE 147° lags HATY 182°

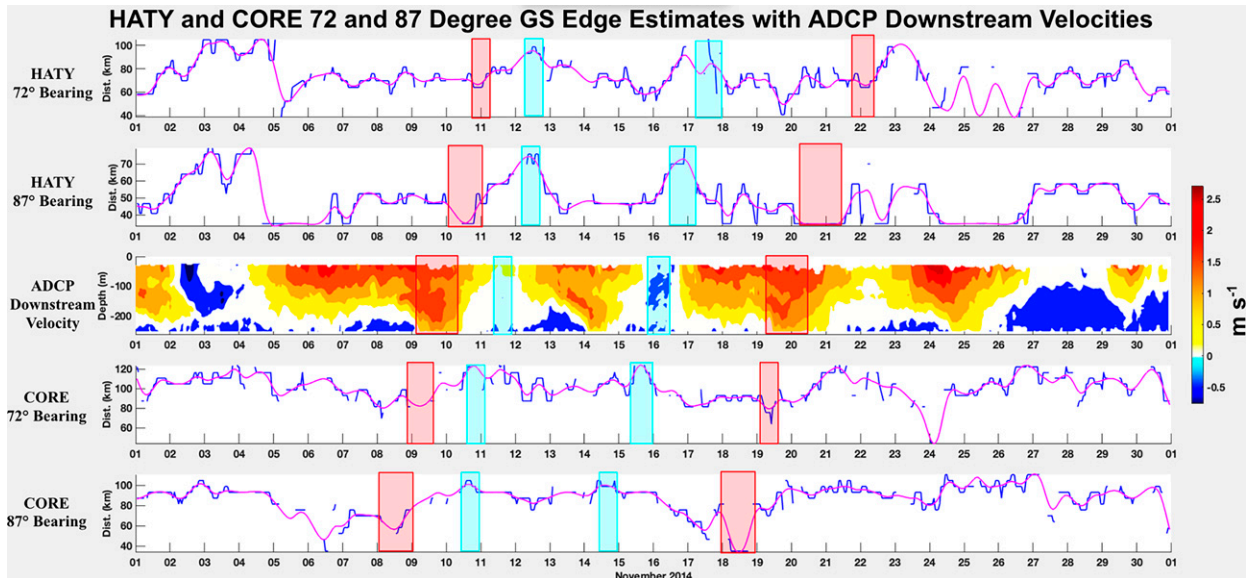


FIG. 13. Edge range estimates from (top to bottom) HATY 72°, HATY 87°, CORE 72°, and CORE 87°, as compared to (middle) downstream velocity as a function of depth and time from the OE ADCP. The panels are arranged from (bottom) south to (top) north; see Fig. 6 for map view. Raw range estimates (blue) are overlain with 24-h cubic spline curves. Pink shading denotes meander crests and blue shading denotes meander troughs. Note the consistent downstream propagation rate of meander features.

(Fig. 13, blue rectangles). The same trough is measured downstream as an increase in distance on the HATY 72° and 87° bearings on 12 and 13 November. Immediately following the trough passage, another crest manifests itself in the observations. On 18 November, a 40-km reduction in distance to the GS edge along the CORE 87° bearing (Fig. 13, red rectangles) and a lesser reduction in range along the CORE 72° bearing, perhaps because of the difference in GS orientation relative the bearing, appear to accompany the largest increase in downstream velocities throughout the water column at the ADCP between the 19 and 20 November. The entire crest passage is well represented in the reduction of distance to the GS edge along the HATY 87° and 72° bearings thereafter between the 24 and 27 November.

Anticorrelations of near-surface current speeds from the ADCP with range to the GS edge along CORE 87°, CORE 72°, HATY 87°, and HATY 72°, are 0.58, 0.67, 0.71, and 0.63, respectively. The highest correlations are from the two bearings, CORE 72° and HATY 87°, nearest the ADCP. The correlations lead by -27 and -14 h for the CORE 87° and 72° bearings upstream of the ADCP and lag by 9 and 17 h for the HATY 87° and 72° bearings downstream of the ADCP. The coherence between separate radar bearings and the changes in downstream velocities caused by several GS meander passages on the ADCP provides further evidence to substantiate the method's efficacy.

4. Discussion

The method presented herein provides new insights about GS structure and dynamics off Cape Hatteras in a meander transition region. It is informative to compare method estimates of GS

properties and spatial and temporal variability in the landward edge, CSZ width, and orientation with previous studies in this region for both method evaluation, and to consider new questions the technique offers to address.

The mean GS edge positions along all bearings are close to the 100-m isobath (Fig. 6), varying from -6 km shoreward to 16 km seaward of the isobath (Table 2). The mean GS front estimated using 4 years of satellite SSTs and Naval Oceanographic Office GS frontal charts lies 19.2 km offshore of the 100-m isobath just south of Cape Hatteras, with a standard deviation of 19.5 km (Glenn and Ebbesmeyer 1994). As shown in Fig. 12, the mean HFR jet axis positions lie along the 0.4-m contour of absolute dynamic topography for the month, consistent with the finding in Zeng and He (2016) that this contour well represented the Gulf Stream core location as it flows along the SAB directly upstream of Cape Hatteras. The one radar edge mean shoreward of the 100-m isobath is made along the CORE 72° bearing (Fig. 6). This shoreward mean is likely caused by the more uncertain radar estimates most distant from the CORE site where the signal to noise ratio for these returns is lower than along the less-distant estimates on the other bearings. It is possible but less likely that it is caused by a shoreward shift in the GS path during November 2014. Previous studies here indicate this is not unphysical but a less likely GS edge location (Andres 2016; Glenn and Ebbesmeyer 1994).

Variability in range estimates from the radars and 100-m isobath to the edge and jet axis are consistent with previous observations. Using SST imagery, Glenn and Ebbesmeyer (1994) found the shoreward edge of the GS to vary by 30–50 km just south of Cape Hatteras; Miller (1994) finds maximum shifts of ~ 100 km approaching Cape Hatteras from the south. The average standard deviation for all CORE bearings is 13.7 km, while

HATY is 12.4 km. Miller (1994), in an analysis of 12 years of Naval Oceanographic Office GS frontal charts, demonstrated that GS frontal position variability decreases downstream of the Charleston Bump as the GS approaches Cape Hatteras.

Observed meander time scales range from an average of about 7 days just south of the radar focus region (Luther and Bane 1985) to 4.6 days within it, with fluctuations ranging from 2 to 14 days (Glenn and Ebbesmeyer 1994). It is informative to consider the meander propagation speed of 50.8 km day⁻¹ reported by Glenn and Ebbesmeyer (1994) and by Andres (2021) of 40–70 km day⁻¹ in this region with respect to the distances and phase lags between some of the well correlated radar edge estimates. The best correlated edge ranges of the HATY 182° and CORE 87° bearings, Table 2, have propagation speeds of 43.2 and 55.2 km day⁻¹ for the edge range—derived by dividing the distance between the mean edge locations by the lag. Similarly, HATY 167° and CORE 72° bearings, with the same lag in edge ranges, have propagation speeds of 69.6 km day⁻¹. Notably, propagation speed estimates between HATY 72°/87° edge estimates increase to 136.8 km day⁻¹. This is a known meander transition region. Meanders propagating downstream from the Charleston Bump diminish nearly completely in amplitude as they approach the GS separation point from the continental margin at Cape Hatteras, and lower-frequency meanders grow and increase in amplitude downstream to the northeast (Savidge 2004). The doubling of radar meander propagation speed here relative to those estimates made upstream warrants further investigation.

Meander propagation coherence observed in the independent measurements from both radars and the ADCP (Fig. 13) provides confidence in the method and hints at further insights that can be gleaned from applying this method to a longer HFR time series. The phasing of meander crests (troughs) seen as reduced (increased) distances to the GS edge along HFR bearings and increased (decreased) near-surface downstream velocities on the ADCP as they propagate through the measurement region provides a new method to frequently and consistently measure the variability in this important meander transition region—suggesting this method could provide insights about potential linkages between upstream and downstream GS meander regimes. The saw-toothed meander pattern seen by Bane et al. (1981) south of Cape Hatteras is also apparent in the HFR and ADCP observations here. Specifically, the time from crest to trough is much greater than that from trough to crest, resulting in asymmetries in the downstream velocity structure. Strong downstream currents occupy an increasing portion of the water column as a crest approaches, and a decreasing fraction as a trough approaches.

The method's mean CSZ width metric estimates vary from 29 to 32 km along all eight bearings, where the width is defined as the distance from the greatest radial gradient to the greatest radial velocity. The CSZ width along the eastern seaboard has been shown to range from ~20 km (~10 km in a jet coordinate frame) (Archer et al. 2017) and 33 km (Schmitz 1996) in the Florida Straits to 60 km northeast of Cape Hatteras near 73°W (Halkin and Rossby 1985), where the width was determined to be the distance from 20 cm s⁻¹ velocities at the western GS edge to the maximum GS velocity (J. Bane 2012, personal communication). The difference in definition may account for

the algorithm estimate being about half the historical one, although the historical estimate is north of Cape Hatteras where the GS has separated from the continental margin.

The most uncertain estimates made by the method are those of GS orientation because they are quite sensitive to the radar bearing relative to the GS orientation, and require combining estimates from two radar bearings that differ by 15°. Intercomparison between estimates separated by a significant along-stream distance are challenging in a region where meanders decrease in amplitude as they approach Cape Hatteras, then reform as the GS separates from the continental margin. Comparisons between estimates at closer proximity to each other reduce this uncertainty, but are complicated by the nearly collocated range estimates being made along bearings that are nearly perpendicular to each other, and the estimate sensitivity to GS orientation. Cross correlations between orientation estimates were less than 0.40, and were not included in Table 2. However, there is much variability in GS orientation in this region, which likely contributes to the low correlations seen at different radar bearing pairs that are spaced ~50–100 km apart.

5. Conclusions and future work

A method has been developed that uses an individual radar's radial velocity field to make consistent and frequent estimates of GS edge location, jet axis location, and orientation. The method has been applied to two radar installations, located on the Core Banks and at Buxton, to yield GS characteristics along eight radial bearings using measurements from November 2014. Although the radars make hourly measurements, they are challenged by noise, and higher uncertainties and lower resolution at greater ranges—thus, HATY tended to have higher quality estimates than CORE. Hourly radial measurements were smoothed with a 24-h low-pass filter to eliminate much of the noise in range estimates; hence, the estimates have temporal resolution of about a day. Comparisons of independent estimates of mean GS position from SSH and those made by individual radars demonstrate a high correlation between measurements that are nearly collocated, and substantiate the accuracy of this method. The method provides a new technique to study GS variability.

Comparisons between the results of the method presented, previous studies in the literature, and other measurements made as part of this study suggest that despite periods of high noise and greater uncertainty in radar radial surface currents, this method provides a valuable new tool for understanding GS variability on daily and longer time scales, offering to contribute to ongoing GS forecasting efforts (Silver et al. 2021). Bearings chosen for analysis are sensitive to the time over which the method is applied; for example, analyzing a week or a day during the same month causes selected analysis bearings for each radar to change slightly. Attention will be given in the future to choosing the time period and duration over which to run the algorithm, consistent with data quality over the study period.

This method is being applied to quality-controlled HFR data (Haines et al. 2017) to measurements from CORE and HATY radials from 2017 to 2018, a period when a large observing array was deployed in the region. The longer time series provides for more robust comparisons with independent observations and

further evaluation of the efficacy of the algorithm, and its ability to accurately determine long-term-mean GS position, CSZ width, and orientation.

Acknowledgments. We gratefully acknowledge SECOORA support to maintain the radar systems on the North Carolina Outer Banks, the North Carolina Renewable Ocean Energy Program for funding the ADCP measurements and CORE radar purchase, and Josh Kohut and Lu Han for their assistance. The authors thank the reviewers for their time.

Data availability statement. Data will be made available by the corresponding author upon request.

REFERENCES

- Andres, M., 2016: On the recent destabilization of the Gulf Stream path downstream of Cape Hatteras. *Geophys. Res. Lett.*, **43**, 9836–9842, <https://doi.org/10.1002/2016GL069966>.
- , 2021: Spatial and temporal variability of the Gulf Stream near Cape Hatteras. *J. Geophys. Res. Oceans*, **126**, e2021JC017579, <https://doi.org/10.1029/2021JC017579>.
- Archer, M. R., L. K. Shay, and W. E. Johns, 2017: The surface velocity structure of the Florida Current in a jet coordinate frame. *J. Geophys. Res. Oceans*, **122**, 9189–9208, <https://doi.org/10.1002/2017JC013286>.
- , S. R. Keating, M. Roughan, W. E. Johns, R. Lumpkin, F. J. Beron-Vera, and L. K. Shay, 2018: The kinematic similarity of two western boundary currents revealed by sustained high-resolution observations. *Geophys. Res. Lett.*, **45**, 6176–6185, <https://doi.org/10.1029/2018GL078429>.
- Bane, J. M., Jr., D. A. Brooks, and K. R. Lorenson, 1981: Synoptic observations of the three-dimensional structure and propagation of Gulf Stream meanders along the Carolina continental margin. *J. Geophys. Res.*, **86**, 6411–6425, <https://doi.org/10.1029/JC086iC07p06411>.
- Barrick, D. E., M. W. Evans, and B. L. Weber, 1977: Ocean surface currents mapped by radar. *Science*, **198**, 138–144, <https://doi.org/10.1126/science.198.4313.138>.
- Bourg, N., and A. Molcard, 2021: Northern boundary current variability and mesoscale dynamics: A long-term HF radar monitoring in the north-western Mediterranean Sea. *Ocean Dyn.*, **71**, 851–870, <https://doi.org/10.1007/s10236-021-01466-9>.
- Brooks, D. A., and J. M. Bane, 1983: Gulf Stream meanders off North Carolina during winter and summer 1979. *J. Geophys. Res.*, **88**, 4633–4650, <https://doi.org/10.1029/JC088iC08p04633>.
- Churchill, J. H., and T. J. Berger, 1998: Transport of middle Atlantic Bight shelf water to the Gulf Stream near Cape Hatteras. *J. Geophys. Res.*, **103**, 30605–30621, <https://doi.org/10.1029/98JC01628>.
- Emery, B. M., L. Washburn, and J. A. Harlan, 2004: Evaluating radial current measurements from CODAR high-frequency radars with moored current meters. *J. Atmos. Oceanic Technol.*, **21**, 1259–1271, [https://doi.org/10.1175/1520-0426\(2004\)021<1259:ERCMF6>2.0.CO;2](https://doi.org/10.1175/1520-0426(2004)021<1259:ERCMF6>2.0.CO;2).
- Frankignoul, C., G. de Coëtlogon, T. M. Joyce, and S. Dong, 2001: Gulf Stream variability and ocean–atmosphere interactions. *J. Phys. Oceanogr.*, **31**, 3516–3529, [https://doi.org/10.1175/1520-0485\(2002\)031<3516:GSVAOA>2.0.CO;2](https://doi.org/10.1175/1520-0485(2002)031<3516:GSVAOA>2.0.CO;2).
- Fuglister, F. C., 1951: Multiple currents in the Gulf Stream system. *Tellus*, **3**, 230–233, <https://doi.org/10.3402/tellusa.v3i4.8661>.
- Gangopadhyay, A., P. Cornillon, and D. R. Watts, 1992: A test of the Parsons–Veronis hypothesis on the separation of the Gulf Stream. *J. Phys. Oceanogr.*, **22**, 1286–1301, [https://doi.org/10.1175/1520-0485\(1992\)022<1286:ATOTPH>2.0.CO;2](https://doi.org/10.1175/1520-0485(1992)022<1286:ATOTPH>2.0.CO;2).
- Glenn, S. M., and C. C. Ebbesmeyer, 1994: Observations of Gulf Stream frontal eddies in the vicinity of Cape Hatteras. *J. Geophys. Res.*, **99**, 5047–5055, <https://doi.org/10.1029/93JC02787>.
- Gula, J., M. J. Molemaker, and J. C. McWilliams, 2015: Gulf Stream dynamics along the southeastern U.S. seaboard. *J. Phys. Oceanogr.*, **45**, 690–715, <https://doi.org/10.1175/JPO-D-14-0154.1>.
- Haines, S., H. Seim, and M. Muglia, 2017: Implementing quality control of high-frequency radar estimates and application to Gulf Stream surface currents. *J. Atmos. Oceanic Technol.*, **34**, 1207–1224, <https://doi.org/10.1175/JTECH-D-16-0203.1>.
- Halkin, D., and T. Rossby, 1985: The structure and transport of the Gulf Stream at 73°W. *J. Phys. Oceanogr.*, **15**, 1439–1452, [https://doi.org/10.1175/1520-0485\(1985\)015<1439:TSATOT>2.0.CO;2](https://doi.org/10.1175/1520-0485(1985)015<1439:TSATOT>2.0.CO;2).
- Hall, M. M., and H. L. Bryden, 1985: Profiling the Gulf Stream with a current meter mooring. *Geophys. Res. Lett.*, **12**, 203–206, <https://doi.org/10.1029/GL012i004p00203>.
- Hogg, N. G., 1992: On the transport of the Gulf Stream between Cape Hatteras and the Grand Banks. *Deep-Sea Res.*, **39A**, 1231–1246, [https://doi.org/10.1016/0198-0149\(92\)90066-3](https://doi.org/10.1016/0198-0149(92)90066-3).
- Johns, W. E., T. J. Shay, J. M. Bane, and D. R. Watts, 1995: Gulf Stream structure, transport, and recirculation near 68°W. *J. Geophys. Res.*, **100**, 817–838, <https://doi.org/10.1029/94JC02497>.
- Joyce, T. M., C. Deser, and M. A. Spall, 2000: The relation between decadal variability of subtropical mode water and the North Atlantic oscillation. *J. Climate*, **13**, 2550–2569, [https://doi.org/10.1175/1520-0442\(2000\)013<2550:TRBDVO>2.0.CO;2](https://doi.org/10.1175/1520-0442(2000)013<2550:TRBDVO>2.0.CO;2).
- Kelly, K. A., 1991: The meandering Gulf Stream as seen by the Geosat altimeter: Surface transport, position, and velocity variance from 73° to 46°W. *J. Geophys. Res.*, **96**, 16721–16738, <https://doi.org/10.1029/91JC01380>.
- , and D. R. Watts, 1994: Monitoring Gulf Stream transport by radar altimeter and inverted echo sounders. *J. Phys. Oceanogr.*, **24**, 1080–1084, [https://doi.org/10.1175/1520-0485\(1994\)024<1080:MGSTBR>2.0.CO;2](https://doi.org/10.1175/1520-0485(1994)024<1080:MGSTBR>2.0.CO;2).
- Kirincich, A. R., T. De Paolo, and E. Terrill, 2012: Improving HF radar estimates of surface currents using signal quality metrics, with application to the MVCO high-resolution radar system. *J. Atmos. Oceanic Technol.*, **29**, 1377–1390, <https://doi.org/10.1175/JTECH-D-11-00160.1>.
- Lee, T. N., J. A. Yoder, and L. P. Atkinson, 1991: Gulf Stream frontal eddy influence on productivity of the southeast US continental shelf. *J. Geophys. Res.*, **96**, 22191–22205, <https://doi.org/10.1029/91JC02450>.
- Liu, Y., R. H. Weisberg, C. R. Merz, S. Lichtenwalner, and G. J. Kirkpatrick, 2010: HF radar performance in a low-energy environment: CODAR SeaSonde experience on the West Florida Shelf. *J. Atmos. Oceanic Technol.*, **27**, 1689–1710, <https://doi.org/10.1175/2010JTECHO720.1>.
- Luther, M. E., and J. M. Bane Jr, 1985: Mixed instabilities in the Gulf Stream over the continental slope. *J. Phys. Oceanogr.*, **15**, 3–23, [https://doi.org/10.1175/1520-0485\(1985\)015<0003:MIITGS>2.0.CO;2](https://doi.org/10.1175/1520-0485(1985)015<0003:MIITGS>2.0.CO;2).
- Meinen, C. S., D. S. Luther, and M. O. Baringer, 2009: Structure, transport and potential vorticity of the Gulf Stream at 68°W: Revisiting older data sets with new techniques. *Deep-Sea Res. I*, **56**, 41–60, <https://doi.org/10.1016/j.dsr.2008.07.010>.
- Menelle, M., G. Auffray, F. Jangal, V. Bazin, and B. Urbani, 2008: HF-surface wave radar: First results for sea state studies.

- Proc. Seventh WSEAS Int. Conf. on Application of Electrical Engineering*, Trondheim, Norway, WSEAS, 27–30.
- Miller, J. L., 1994: Fluctuations of Gulf Stream frontal position between Cape Hatteras and the Straits of Florida. *J. Geophys. Res.*, **99**, 5057–5064, <https://doi.org/10.1029/93JC03484>.
- Muglia, M., H. Seim, and P. Taylor, 2020: Gulf Stream marine hydrokinetic energy off Cape Hatteras, North Carolina. *Mar. Technol. Soc. J.*, **54**, 24–36, <https://doi.org/10.4031/MTSJ.54.6.4>.
- Myers, R. A., and K. Drinkwater, 1989: The influence of Gulf Stream warm core rings on recruitment of fish in the north-west Atlantic. *J. Mar. Res.*, **47**, 635–656, <https://doi.org/10.1357/002224089785076208>.
- Paduan, J. D. and H. C. Graber, 1997: Introduction to high-frequency radar: Reality and myth. *Oceanography*, **10** (2), 36–39, <https://doi.org/10.5670/oceanog.1997.18>.
- Richardson, P. L., 1985: Average velocity and transport of the Gulf Stream near 55W. *J. Mar. Res.*, **43**, 83–111, <https://doi.org/10.1357/002224085788437343>.
- Savidge, D. K., 2004: Gulf Stream meander propagation past Cape Hatteras. *J. Phys. Oceanogr.*, **34**, 2073–2085, [https://doi.org/10.1175/1520-0485\(2004\)034<2073:GSMPPC>2.0.CO;2](https://doi.org/10.1175/1520-0485(2004)034<2073:GSMPPC>2.0.CO;2).
- , and J. M. Bane Jr., 2001: Wind and Gulf Stream influences on along-shelf transport and off-shelf export at Cape Hatteras, North Carolina. *J. Geophys. Res.*, **106**, 11 505–11 527, <https://doi.org/10.1029/2000JC000574>.
- , and J. A. Austin, 2007: The Hatteras Front: August 2004 velocity and density structure. *J. Geophys. Res.*, **112**, C07006, <https://doi.org/10.1029/2006JC003933>.
- Schmitz, W. J., Jr., 1996: On the world ocean circulation. Volume 1. Some global features/North Atlantic circulation. Woods Hole Oceanographic Institution Rep. WHOI-96-03, 148 pp., <https://doi.org/10.1575/1912/355>.
- Shay, L. K., H. E. Seim, D. Savidge, R. Styles, and R. H. Weisberg, 2008: High frequency radar observing systems in SEACOOS: 2002–2007 lessons learned. *Mar. Technol. Soc. J.*, **42**, 55–67, <https://doi.org/10.4031/002533208786842435>.
- Silver, A., A. Gangopadhyay, G. Gawarkiewicz, A. Taylor, and A. Sanchez-Franks, 2021: Forecasting the Gulf Stream path using buoyancy and wind forcing over the North Atlantic. *J. Geophys. Res. Oceans*, **126**, e2021JC017614, <https://doi.org/10.1029/2021JC017614>.
- Taylor, J., 1997: *Introduction to Error Analysis, the Study of Uncertainties in Physical Measurements*. 2nd ed. University Science Books, 343 pp.
- Watts, D. R., K. L. Tracey, J. M. Bane, and T. J. Shay, 1995: Gulf Stream path and thermocline structure near 74°W and 68°W. *J. Geophys. Res.*, **100**, 18291–18312, <https://doi.org/10.1029/95JC01850>.
- Zeng, X., and R. He, 2016: Gulf Stream variability and a triggering mechanism of its large meander in the South Atlantic Bight. *J. Geophys. Res. Oceans*, **121**, 8021–8038, <https://doi.org/10.1002/2016JC012077>.
- Zhang, W. G., and G. G. Gawarkiewicz, 2015: Dynamics of the direct intrusion of Gulf Stream ring water onto the mid-Atlantic Bight shelf. *Geophys. Res. Lett.*, **42**, 7687–7695, <https://doi.org/10.1002/2015GL065530>.